

Models of X-ray and γ -ray emission from Seyfert galaxies

Roland Svensson

Stockholm Observatory, S-133 36 Saltsjöbaden, Sweden
Internet: svensson@astro.su.se

Received December 15, 1995; accepted February 4, 1996

Abstract. X-ray and γ -ray observations of Seyfert 1 galaxies are briefly reviewed. Both thermal and non-thermal model for X-ray and γ -ray emission are discussed. Particular attention is given to various disc-corona models including both homogeneous and inhomogeneous (patchy) corona models. Recent work on exact radiative transfer in such geometries are reviewed.

Key words: accretion disks – galaxies: Seyfert – gamma rays: theory – radiative transfer – scattering – X-rays: galaxies

1. X-ray and γ -ray spectra of Seyfert 1 galaxies

By combining observations in different energy bands, a picture has emerged where the overall shapes of the X-ray and γ -ray spectra of different Seyfert 1 galaxies are similar. The only Seyfert 1 galaxy for which the broad band X- and γ -ray spectrum is well determined is IC 4329A (Madejski et al. 1995). Combined *ROSAT*, *Ginga* and OSSE data are shown in Fig. 1. The observations were modelled by Madejski et al. (1995), Zdziarski et al. (1994), and Magdziarz & Zdziarski (1995). The spectrum consists of two components: 1) an intrinsic power law of slope $\alpha_{\text{int}} \approx 0.9$ with an exponential cutoff energy of about 300 keV (dashed curve in Fig. 1), and 2) a reflection component caused by cold reflecting matter subtending a solid angle $\sim 1 - 2\pi$ as viewed from the X-ray source (dotted curve in Fig. 1). The reflection component peaks at about 30 keV causing the overall 2-18 keV spectral slope to be considerably flatter, $\alpha_{2-18} \approx 0.7$ and the apparent cutoff energy to be smaller, ≈ 50 keV.

The average X/ γ -spectrum for four Seyfert 1s using nonsimultaneous *Ginga* and OSSE data (23 *Ginga* spectra and 8 OSSE spectra) shows similar properties as the spectrum for IC 4329A (Zdziarski et al. 1995). The same holds for the nonsimultaneous average *EXOSAT*/OSSE spectrum for seven Seyfert 1s using 31 *EXOSAT* and 18 OSSE observations (Gondek et al. 1996). These spectra

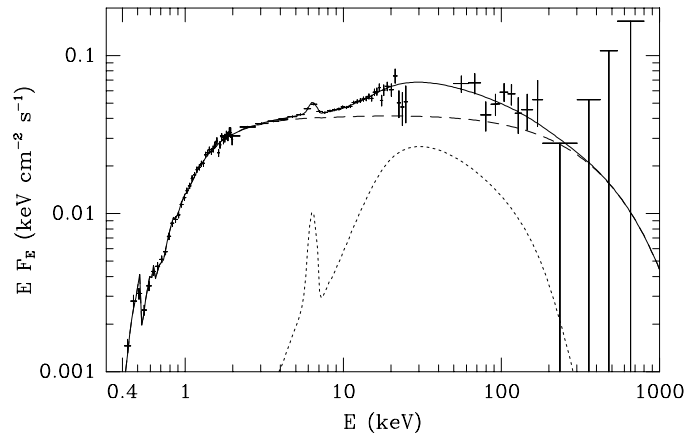


Fig. 1. The broad band spectrum (crosses) of IC 4329A from *ROSAT*, *Ginga*, and OSSE (Madejski et al. 1995). The dashed curve shows the intrinsic spectrum incident on the cold matter, the dotted curve is the reflected component, and the solid curve is the sum. From Magdziarz & Zdziarski (1995).

are consistent with the average spectrum of these Seyfert 1s from *HEAO-1* A4 (Gondek et al. 1996) and with the upper limits of all Seyferts from COMPTEL (Maisack et al. 1995).

Larger samples exist within narrower spectral ranges using a single experiment. These samples show spectra consistent with the smaller samples above. For example, 60 *Ginga* spectra of 27 Seyferts show $\alpha_{\text{int},2-18} \approx 0.95$ and the overall $\alpha_{2-18} \approx 0.73$, each having a dispersion of about 0.15 (Nandra & Pounds 1994).

The brightest Seyfert 1 (or 1.5), NGC 4151, once considered a prototype for Seyfert 1s, has now turned out to have unusual X-ray properties. In the 2-18 keV *Ginga*-range, the spectral index, α_{2-18} , varies in the range 0.3-0.7 instead of having the canonical Seyfert value of 0.7. The harder the spectrum is, the weaker is the 2-18 keV flux, and the spectrum seems to pivot around 100 keV. And indeed, OSSE observations during 5 viewing periods from 1991-1994 show that the OSSE flux is essentially constant (25 % day-to-day variability; Johnson et al 1996). Further-

more, the OSSE observations show that the spectrum cuts off at about 50 keV, much less than the canonical 300 keV value. Finally, there seems to be no reflection component. NGC 4151 is clearly a freak object which requires special consideration to fit into the unified scheme of Seyfert galaxies.

2. Outstanding questions regarding the X-ray emitting regions in Seyfert 1 galaxies

The obvious question is of course which radiation process generates the X-ray continuum. It is commonly believed that Compton scattering by energetic electrons, either mildly relativistic thermal electrons or highly relativistic nonthermal electrons, Compton scatter soft UV-photons into the X-ray range.

Then there is the question of geometry, i.e. the spatial distribution of hot X-ray generating electrons and of cold ($T < 10^6$ K) reflecting matter. Possible geometries include a cold slab surrounded either by plane parallel coronal slabs of hot electrons, or by coronal patches (active regions) of unknown geometries.

Finally, there is the question whether it is thermal or nonthermal electrons or both that account for the X-ray emission. This question might be answered if the spectrum above a few hundred keV was known with certainty, but the best available spectrum of the brightest typical Seyfert 1, IC 4329A, does not have sufficient signal to noise at such energies. The spectrum of IC 4329A can be fit with both thermal and nonthermal models (Zdziarski et al. 1994).

The nonthermal models studied in the 1980s have several attractive features (for review, see Svensson 1994). In particular, it was predicted already in 1985 (Svensson 1986) that the pair cascades in the nonthermal models give rise to an X-ray spectrum with $\alpha_{\text{int},2-18} \approx 0.9 - 1.0$ in contradiction to the overall slope of $\alpha_{2-18} \approx 0.7$ but in agreement with the intrinsic spectral slope later found by *Ginga* (e.g. Nandra & Pounds 1994).

Due to the non-detections by COMPTEL and the high energy cutoffs indicated by OSSE, attention has recently been focused on the thermal models.

3. Geometry of the X-ray source

In the unified model for Seyfert galaxies (e.g. Antonucci 1993), we are directly viewing the central X-ray source and broad line region in Seyfert 1 galaxies, but our line-of-sight passes through an optically opaque molecular torus in Seyfert 2 galaxies. In standard accretion disk scenarios for the central X-ray source, the unified models imply that our viewing angle (i.e. the angle between the disk normal and the line-of-sight) is less than the half-opening angle of the ionization cone. Half-opening angles inferred from observations are typically 30-40 degrees, which means that in Seyfert 1s we are viewing the accretion disk from directions that are closer to face-on than to edge-on.

In principle, the central X-ray source could have spherical symmetry with the source of UV-photons being small cold clouds uniformly distributed throughout the X-ray source. In this case, radiation models invoking spherical symmetry would be applicable (e.g., Ghisellini & Haardt 1994, Skibo et al. 1995; Pietrini & Krolik 1995). In some models, the central X-ray source is quasi-spherical but the UV-source is anisotropic. Here, the X-ray source can either be a hot two-temperature accretion disk in local thermal balance (Shapiro, Lightman, & Eardley 1976) or a two-temperature ion torus (Rees et al. 1982, recently rejuvenated as advection dominated accretion flows, e.g. Abramowicz et al. 1995, where the connections between the two types of hot disks with other disk solutions are elucidated). The UV-source may then be the standard cold Shakura-Sunyaev disk located beyond some transition radius. This anisotropy of the UV-photons breaks the spherical symmetry. Then detailed radiative transfer calculations of how the UV-photons penetrate the hot disk are required in order to determine the emerging X-ray spectrum of Comptonized UV-photons at different viewing angles. This problem has not yet been solved.

The most commonly used scenario is the two-phase disk-corona model (e.g., Haardt & Maraschi 1991, 1993) in which a hot X-ray emitting corona is located above the cold UV-emitting disk of the canonical black hole model for AGNs. The power law X-ray spectrum is generated by thermal Comptonization of the soft UV-radiation. About half of the X-rays enters and is reprocessed by the cold disk, emerging mostly as black body disk radiation in the UV. Haardt & Maraschi (1991) emphasized the coupling between the two phases due to the reprocessing, as the soft disk photons influence the cooling of the corona. They showed that nearly all power must be dissipated in the corona in order to have $\alpha_{\text{int}} \sim 0.9 - 1$. A consequence of this is that the soft disk luminosity, L_s , is of the same order as the hard X-ray luminosity, L_h . The disk-corona scenario is highly anisotropic as the UV-photons enter the corona from below only.

Observations show that L_s may be several times larger than L_h , in contradiction to the prediction of the uniform two-phase disk-corona model. This led Haardt, Maraschi, & Ghisellini (1994) to propose a patchy disk-corona model, where the corona consists of several localized active regions on the surface of the disk. Internal disk dissipation results in UV-radiation that leaves the disk without entering the active regions, thus enhancing the observed L_s relative to L_h . The patchy corona model is also highly anisotropic as the UV-radiation enters the active regions from below and through the sides.

The full radiative transfer and Comptonization problem in the these geometries has recently been solved (Haardt & Maraschi 1993, Stern et al. 1995b, Poutanen & Svensson 1996). We now turn to discuss the methods and the results.

4. Radiative transfer/Comptonization

Two different methods have been used to solve the full radiative transfer/Comptonization problem in mildly relativistic thermal plasmas accounting for energy and pair balance as well as reprocessing by the cold disk (including angular anisotropy and Klein-Nishina effects).

The first method is based on the Non-Linear Monte Carlo (NLMC) method developed by Stern (1985, 1988) and described in detail in Stern et al (1995a). The Monte Carlo particles (particles and photons) make up the background so the Monte Carlo particles can interact with themselves (e.g. photon-photon pair production) causing nonlinearity. Any geometry can be treated including 2D and 3D geometries, but calculations so far (Stern et al 1995b) have been limited to coronal slabs (1D) or active regions (2D) in the shape of hemispheres or spheres at different elevations above the cold disc. Another advantage is the possibility to divide the region into several zones in order to study the inhomogeneous distributions of, e.g., temperature and pair density. The drawback is that each run takes a few hours on a Sun IPX.

The second method is based on the iterative scattering method (ISM), where the radiative transfer is exactly solved for each scattering order separately (e.g. Sunyaev & Titarchuk 1985, Haardt 1994). The code and its testing are briefly described in Poutanen and Svensson (1996, see also Poutanen 1994; Poutanen & Vilhu 1993). It was shown that the results of the NLMC and the ISM code are in excellent agreement. The ISM code is a 1D code but it can also treat quasi-2D radiative transfer in cylinders/pill boxes and hemispheres. The full Compton scattering matrix is used allowing to solve polarized radiative transfer in thermal relativistic plasmas. Fully angular dependent, polarized Compton reflection is implemented using a Green's matrix (Poutanen, Nagendra & Svensson 1996). The advantage of the ISM code is that it takes 10 minutes or less on a Sun IPX.

5. The Comptonization solution

The two codes have been used to study radiative transfer/Comptonization in pure pair coronae in energy and pair balance. For coronae of a given geometry and in energy balance, there exists a unique $T_e - \tau_T$ relation, where T_e is the volume-averaged coronal temperature and τ_T is a characteristic Thomson scattering optical depth of the coronal region. For slabs, τ_T is the vertical Thomson scattering optical depth. For hemispheres and for spheres, the radial τ_T is averaged over 2π solid angle for hemispheres, and 4π solid angle for spheres.

In Figure 2, this relation is shown for different geometries. The results for slabs are shown by *rectangles*, for hemispheres located on the disk surface by *hemispheres*, for surface spheres located on the disk surface by *underlined spheres*, and for spheres located at heights, $0.5h$, $1h$,

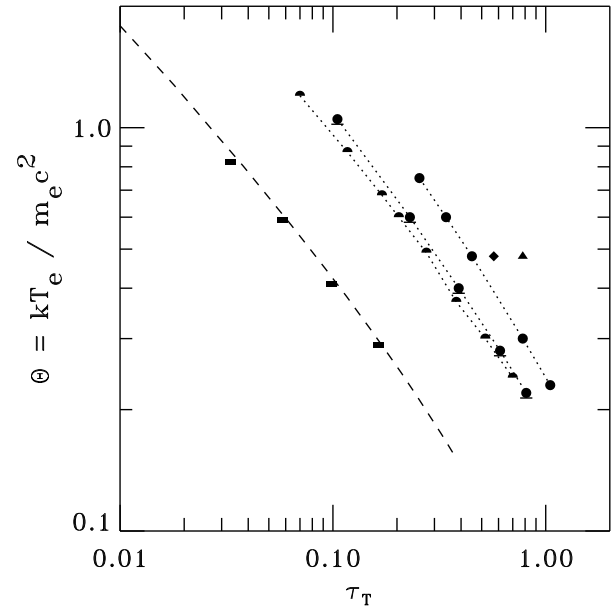


Fig. 2. Dimensionless volume-averaged temperature, $\Theta \equiv kT_e/m_e c^2$, vs. Thomson scattering optical depth, τ_T , for a steady X-ray emitting plasma region on or above a cold disk surface. The plasma Compton scatters reprocessed soft black body photons from the cold disk surface. *Solid rectangles* and *dashed curve* show results from NLMC code and ISM code, respectively, for the case of a plane-parallel slab corona. Results using the NLMC code for individual active pair regions are shown for *hemispheres* located on the disk surface; surface spheres also located on the surface (*underlined spheres*); spheres located at a height of $0.5h$ (*spheres*), $1h$ (*diamond*), and $2h$ (*triangle*), where h is the radius of the sphere. The results for each type of active region are connected by *dotted curves*. The cold disk temperature, $kT_{bb} = 5$ eV. From Stern et al. (1996).

and $2h$, by *spheres*, *diamonds*, and *triangles*, respectively (h is the radius of the sphere). The results for active regions are connected by *dotted curves*. For comparison we also show the slab results from Stern et al. 1995b using the ISM code (*dashed curve*). Each curve is characterized by an almost constant generalized Kompaneets parameter, $y \equiv \tau_T(1 + \tau_T)(4\Theta + 16\Theta^2)$, where $\Theta \equiv kT_e/m_e c^2$. The larger the soft photon starvation (i.e. the fewer the number of reprocessed soft photons reentering the coronal region), the larger is y . There is very good agreement between the slab results from the NLMC and the ISM codes, which tests the accuracy of both codes and methods.

6. Pair balance and the compactness

Solving the pair balance for the combinations of (Θ, τ_T) obtained in § 5 gives a unique dissipation compactness, ℓ_{diss} (see Ghisellini & Haardt 1994 for a discussion). Here, the local dissipation compactness, $\ell_{diss} \equiv (L_{diss}/h)(\sigma_T/m_e c^3)$, characterizes the dissipation with

L_{diss} being the power providing uniform heating in a cubic volume of size h in the case of a slab of height h , or in the whole volume in the case of an active region of size h . Figures 3 shows the Θ vs. ℓ_{diss} relation obtained with the NLMC code for different geometries and for $kT_{\text{bb}} = 5$ eV. Notations are the same as in Figure 2. The slab results with the ISM codes are also shown by the dashed curve. The parameter space to the right of respective curve is forbidden as pair balance cannot be achieved, and the parameter space to the left would contain solutions where the background coronal plasma dominates over the pairs, i.e. “pair free” solutions (e.g. Svensson 1984, HM93).

From Figure 3 we find that at a given Θ the ARs have a larger ℓ_{diss} than the slabs. This is due to the longer escape times in slabs. In a local cubic volume in slabs, the four vertical surfaces act effectively as “reflecting” surfaces increasing the radiation energy density in the volume as compared to the ARs where the radiation escapes freely through the surface of the AR volume.

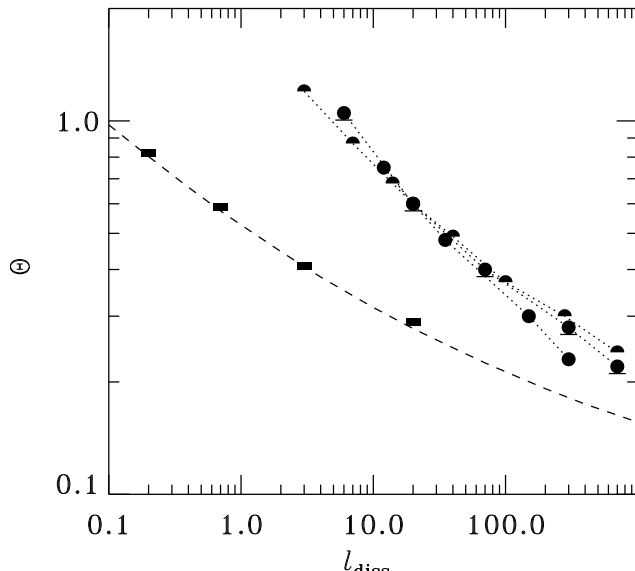


Fig. 3. Dimensionless temperature, $\Theta \equiv kT_e/m_ec^2$, vs. dissipation compactness, $\ell_{\text{diss}} \equiv (L_{\text{diss}}/h) (\sigma_T/m_ec^3)$, for a steady X-ray emitting pair plasma in pair and energy balance located on or above a cold disk surface. Same symbols and notation as in Fig. 2. The parameter space to the right of respective curves is forbidden as pair balance cannot be achieved, and the parameter space to the left would contain solutions where the background coronal plasma dominates over the pairs, i.e. “pair free” solutions (e.g. Svensson 1984, HM93). The soft photons from the cold disk are assumed to have $kT_{\text{bb}} = 5$ eV. From Stern et al. (1996).

7. Anisotropy effects

Figure 4 shows the “face-on” emerging spectrum for a hemisphere with $\ell_{\text{diss}} = 20$ and $kT_{\text{bb}} = 5$ eV with the reflected component subtracted. The *solid curve* is the sum of the reprocessed soft black body spectrum and the Comptonized spectrum. The “face-on” spectrum is averaged over viewing angles $0.6 < \cos \theta < 1$. The numbered *dotted curves* show spectral profiles of the different scattering orders. As noted by Haardt (1993) and HM93, the first scattering order is significantly reduced in face-on directions due to anisotropic Compton scattering when Θ is mildly relativistic. This deficiency at low energies causes an *anisotropy break* close to the peak of the second scattering order. Below the anisotropy break, the spectrum is a power law with an *anisotropy slope*, α_{aniso} , that is harder than the standard *isotropy slope*, α_{iso} , above the break. It is the standard isotropy slope, α_{iso} , that has been fitted with several analytical expressions that are functions of Θ and τ_T (e.g., Zdziarski 1985, Titarchuk 1994). “Edge-on” spectra have a much weaker reflection component and no anisotropy break.

8. Spectra from active pair regions: hemispheres

Figure 5 shows emerging “face-on” spectra from hemispheres at different ℓ_{diss} for $kT_{\text{bb}} = 5$ eV. We have $\alpha_{\text{aniso}} \approx 0.77$ while $\alpha_{\text{iso}} \approx 1.09$. The anisotropy break is therefore about 0.3. The anisotropy break moves through the 2-18 keV range for $\ell_{\text{diss}} \approx 10-100$, and thus α_{2-18} is smaller than unity for ℓ_{diss} less than 100. At this low kT_{bb} the first Compton order hardly extends into the 2-18 keV range and there is little discreteness effect on the behaviour of α_{2-18} .

9. Diagnostics Using Compactness and Ginga Slopes

The least square overall spectral slope, α_{2-18} , for the 2-18 keV range were determined and are displayed in Figure 6 as a function of the dissipation compactness, ℓ_{diss} , for different geometries. The right panel of Figure 6 shows the observed distribution of α_{2-18} for *Ginga* spectra from 27 Seyfert galaxies (Nandra & Pounds 1994). The crosses represent 17 Seyfert galaxies that have both been observed by *Ginga* and have known estimates of their X-ray time variability (and thus lower limits of their compactnesses). The true crosses may lie to the right of the plotted ones.

One sees that the observations are more consistent with active surface regions (such as hemispheres) than with slabs. Active regions produce spectra covering the *observed ranges* of α_{2-18} ($\approx 0.4 - 0.9$) and cutoff energies ($\sim 2kT_e$) for the *observed range* of compactnesses.

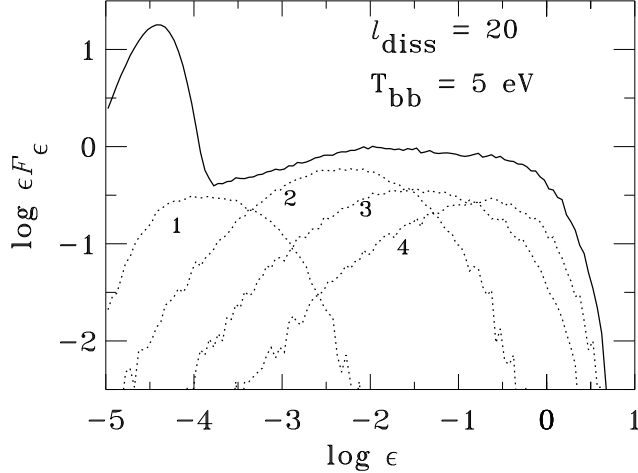


Fig. 4. Emerging spectrum, ϵF_ϵ , where F_ϵ is the energy flux (arbitrary units) and $\epsilon \equiv h\nu/m_e c^2$ from hemisphere with compactness, $l_{\text{diss}} = 20$, and cold disk temperature, $kT_{\text{bb}} = 5$ eV. The spectrum is averaged over viewing angles $0.6 < \cos \theta < 1$. The *solid curve* shows the sum of the Comptonized spectrum from the hemisphere and the reprocessed black body spectrum (the reflection component is not included). The numbered *dotted curves* show the different scattering orders. Note that the first scattering order is significantly reduced due to anisotropic Compton scattering. This deficiency causes an *anisotropy break* close to the peak of the second scattering order. Below the anisotropy break, the spectrum is a power law with an *anisotropy slope* that is harder than the standard *isotropy slope* above the break. From Stern et al. (1996).

10. Conclusions

Have we been able to throw some light upon the outstanding questions discussed in § 2?

Regarding the radiative transfer/Comptonization, the progress has been rapid and it is now possible to use full radiative transfer simulations when fitting X-ray observations, e.g. with XSPEC. As anisotropic effects are very important, i.e. as spectral shapes depend strongly on viewing angle, it will be possible to set constraints on the viewing angle.

The spectra also depend on the geometry of the coronal regions, so observed spectra can be used as diagnostics of the geometry. Presently, it seems that active regions are favoured over homogeneous slab coronae.

There is still no answer to the question whether the radiating electrons (and positrons) are thermal or non-thermal. High quality spectra above 200 keV are needed, and the question may not be settled before the launch of *INTEGRAL*.

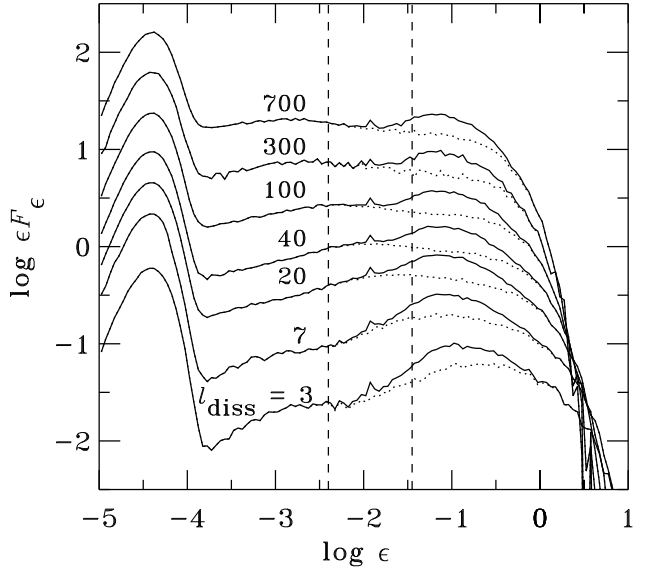


Fig. 5. Emerging “face-on” spectra, ϵF_ϵ , where F_ϵ is the energy flux (arbitrary units) and $\epsilon \equiv h\nu/m_e c^2$, from hemispheres of different compactnesses, l_{diss} and for cold disk temperature, $kT_{\text{bb}} = 5$ eV. The “face-on” spectra are averaged over viewing angles $0.6 < \cos \theta < 1$. The *solid curves* show the total spectrum which is the sum of the Comptonized spectrum from the hemisphere itself (*dotted curves*), the reprocessed black body spectrum, and the reflection component. Vertical *dashed lines* show the 2-18 keV spectral range. The anisotropy break in the face-on spectra moves to lower photon energies as l_{diss} increases. From Stern et al. (1995b).

Acknowledgements. The author thanks the Swedish Natural Science Research Council, which fully supported (including the registration fee) the invited participation in the 3rd Compton Symposium. He also thanks Juri Poutanen for valuable comments.

References

- Antonucci R., 1993, ARA&A 31, 473
- Abramowicz M., Chen X., Kato S., Lasota J. P., Regev O., 1995, ApJ 332, 646
- Ghisellini G., Haardt F., 1994, ApJ 429, L53
- Gondek D., et al., 1996, MNRAS, submitted
- Haardt F., 1993, ApJ 413, 680
- Haardt F., 1994, High Energy Processes in Seyfert Galaxies, Dissertation, SISSA, Trieste
- Haardt F., Maraschi L., 1991, ApJ 380, L51
- Haardt F., Maraschi L., 1993, ApJ 413, 507
- Haardt F., Maraschi L., Ghisellini, G., 1994, ApJ 432, L95
- Johnson W. N., et al., 1996, A&AS, submitted
- Madejski G. M., et al., 1995, ApJ 438, 672
- Magdziarz P., Zdziarski, A. A., 1995, MNRAS 273, 837
- Maisack M., et al., 1995, A&A 298, 400
- Nandra K., Pounds K. A., 1994, MNRAS 268, 405
- Pietrini P., Krolik J. H., 1995, ApJ 447, 526

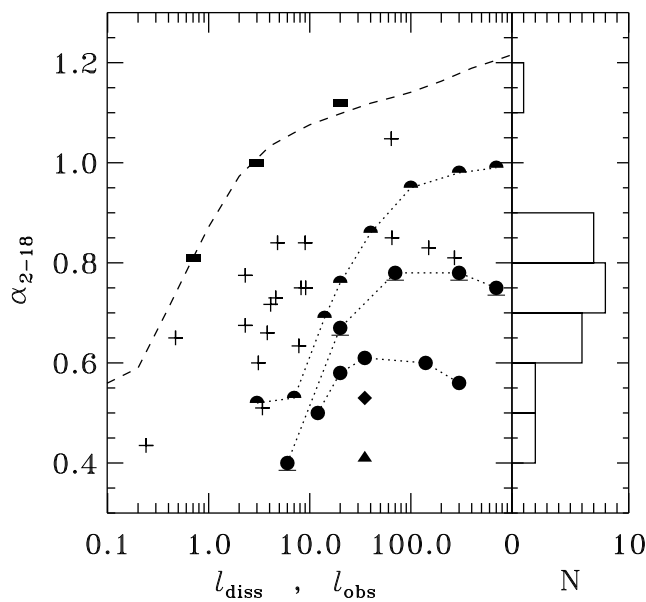


Fig. 6. Overall spectral intensity index, α_{2-18} , least square fitted to the model spectra in the 2-18 keV range vs. the dissipation compactness, l_{diss} . Same notation as in Fig. 2. The spectra from NLMC code were averaged over viewing angles $0.6 < \cos \theta < 1.0$ before determining α_{2-18} with least square fitting. For the ISM code, face-on spectra (at $\cos \theta = 0.887$) were used. The right panel shows the observed distribution of α_{2-18} for *Ginga* spectra from 27 Seyfert galaxies (Nandra & Pounds 1994). The crosses represent 17 Seyfert galaxies that have both been observed by *Ginga* and have known estimates of their X-ray time variability, Δt , and thus of the observed compactness, $l_{\text{obs}} \equiv (L_{\text{obs}}/c\Delta t)(\sigma_{\text{T}}/m_e c^3)$.

Svensson R., 1986, in: Radiation Hydrodynamics in Stars and Compact Objects, IAU Coll. 89, eds. D. Mihalas and K-H. Winkler, Springer, New York
 Svensson R., 1994, ApJS 92, 585
 Titarchuk L., 1994, ApJ 434, 570
 Zdziarski A. A., 1985, ApJ 289, 514
 Zdziarski A. A. et al., 1994, MNRAS 269, L55
 Zdziarski A. A., Johnson W. N., Done C., Smith D., McNaron-Brown, K., 1995, ApJ 438, L63

Poutanen J., 1994, Compton Scattering of Polarized Light in Active Galactic Nuclei and X-Ray Binaries, Dissertation, University of Helsinki
 Poutanen J., Svensson R., 1996, ApJ, in press
 Poutanen J., Vilhu O., 1993, A&A 275, 337
 Poutanen J., Nagendra K. N., Svensson, R., 1996, MNRAS, submitted
 Rees M. J., Begelman M. C., Blandford R. D., Phinney E. S., 1982, Nat 295, 17
 Shapiro S. L., Lightman A. P., Eardley D. N., 1976, ApJ 204, 187
 Skibo J. G., Dermer C. D., Ramaty R., McKinley J. M., 1995, ApJ 446, 86
 Stern B. E., 1985, SvA 29, 306
 Stern B. E., 1988, Nordita/88-51 A, preprint
 Stern B. E., Begelman M. C., Sikora M., Svensson R., 1995a, MNRAS 272, 291
 Stern B. E., Poutanen J., Svensson R., Sikora M., Begelman M. C., 1995b, ApJ 449, L13
 Stern B. E., et al., 1996, in preparation
 Sunyaev R. A., Titarchuk L. G., 1985, A&A 143, 374
 Svensson R., 1984, MNRAS 209, 175